

# Level structure of $^{221}\text{Ac}$ and $^{217}\text{Fr}$ from decay spectroscopy, and reflection asymmetry in $^{221}\text{Ac}$

E. Rey-herme<sup>1</sup>, A. Raggio<sup>2</sup>, M. Vandebrouck<sup>1</sup>, I. Moore<sup>2</sup>, I. Pohjalainen<sup>2</sup>, C. Delafosse<sup>3</sup>, R. de Groote<sup>4</sup>, Z. Ge,<sup>5</sup>  
S. Geldhof<sup>2,6</sup>, M. Hukkanen,<sup>2</sup> A. Kankainen<sup>2</sup>, A. Koszorus,<sup>4</sup> D. Nesterenko<sup>2</sup>, J. Sarén<sup>2</sup>, B. Sulignano<sup>1</sup>,  
Ch. Theisen<sup>1</sup>, D. Thisse<sup>1</sup> and A. P. Weaver<sup>7</sup>

(IGISOL Collaboration)

<sup>1</sup>*Irfu, CEA, Université Paris-Saclay, 91191 Gif-sur-Yvette, France*

<sup>2</sup>*Department of Physics, Accelerator Laboratory, University of Jyväskylä, FIN-40014 Jyväskylä, Finland*

<sup>3</sup>*Université Paris-Saclay, CNRS/IN2P3, IJCLab, 91405 Orsay, France*

<sup>4</sup>*Institute for Nuclear and Radiation Physics, KU Leuven, 3000 Leuven, Belgium*

<sup>5</sup>*GSI Helmholtzzentrum für Schwerionenforschung GmbH, Planckstr. 1, 64291 Darmstadt, Germany*

<sup>6</sup>*Grand Accélérateur National d'Ions Lourds, Bd Henri Becquerel, 14076 Caen, France*

<sup>7</sup>*School of Computing, Engineering and Mathematics, University of Brighton, Brighton BN2 4GJ, United Kingdom*



(Received 8 March 2023; accepted 2 June 2023; published 5 July 2023)

$^{225}\text{Pa}$  and  $^{221}\text{Ac}$  were produced at the IGISOL facility through proton-induced fusion-evaporation reactions and have been studied using  $\alpha$ -particle spectroscopy, as well as  $\alpha$ - $\gamma$  and  $\alpha$ -electron coincidence spectroscopy. The level scheme of  $^{221}\text{Ac}$ , daughter of  $^{225}\text{Pa}$ , and of  $^{217}\text{Fr}$ , daughter of  $^{221}\text{Ac}$  were reconstructed. An interpretation of  $^{221}\text{Ac}$  levels as  $K = 5/2^\pm$  and  $K = 3/2^\pm$  parity-doublet bands is proposed. Such bands appear in reflection-asymmetric models and would be an indication of a static reflection asymmetric shape for  $^{221}\text{Ac}$ .

DOI: [10.1103/PhysRevC.108.014304](https://doi.org/10.1103/PhysRevC.108.014304)

## I. INTRODUCTION

The study of octupole deformation in atomic nuclei has been a hot topic for the past decades [1–3], with substantial theoretical predictions and experimental evidence for reflection-asymmetric shapes in the neutron-deficient actinides [1–12]. The most pronounced deformation in the actinide region is centered around  $^{222}\text{Ra}$  ( $Z = 88$  and  $N = 134$ ) [3]. In addition to the intrinsic interest in understanding nuclear structure, the deformation is linked to the stability of heavy and superheavy nuclei as it can considerably decrease the fission barrier [13,14] and plays a major role in the description of cluster emission [15,16]. Moreover, the collective behavior arising from octupole correlations results in a large enhancement of symmetry-violating nuclear properties, such as the Schiff moment [17,18]. A measurement of this property would help to constrain sources of charge-parity (CP) violation, proposed as necessary ingredients in our understanding of the observed matter-antimatter asymmetry in the universe. We note that further sensitivity may be gained through the study of radioactive molecules incorporating heavy, octupole-deformed nuclei, highlighting a renewed interest in the underlying structure of such nuclei [19].

The odd-mass (odd- $A$ ) actinide nuclei have been extensively studied by Sheline and collaborators in the 1980s and 1990s [20–23], attempting to establish the extent of the static quadrupole-octupole region of deformation in the ground-states of actinide isotopes. For the past 20 years, however, the experimental measurements in the region have been scarce.

In this work, the odd-proton (odd- $Z$ ) neutron-deficient actinide  $^{221}\text{Ac}$  ( $Z = 89$ ) and its daughter nucleus  $^{217}\text{Fr}$  ( $Z = 87$ ) have been studied through the  $\alpha$  decay of  $^{225}\text{Pa}$  ( $Z = 91$ ) and  $^{221}\text{Ac}$ , respectively, with a measurement of the  $\gamma$  rays and

conversion electrons emitted in coincidence.  $^{225}\text{Pa}$  and  $^{221}\text{Ac}$  were produced through a proton-induced fusion-evaporation reaction on a  $^{232}\text{Th}$  ( $Z = 90$ ) target. New results, including six new  $\alpha$  branches and more than 20 new  $\gamma$  rays, were obtained and an interpretation of the level scheme of  $^{221}\text{Ac}$  is proposed.

## II. PREVIOUS RESULTS

### A. $^{225}\text{Pa} \rightarrow ^{221}\text{Ac}$ $\alpha$ decay

The  $\alpha$  decay of  $^{225}\text{Pa}$  has previously been reported in several references [24–29]. The most extensive study [24], published recently, reports seven  $\alpha$ -decay branches with energies, intensities and hindrance factors given in Table I, as well as four  $\gamma$ -ray transitions observed in coincidence for the first time. In this recent work, the authors assign a  $I^\pi = 5/2^-$  to the ground state for both  $^{221}\text{Ac}$  and  $^{225}\text{Pa}$ . For comparison the previous work of Huysse and collaborators had clean  $\alpha$ -energy spectra showing three  $\alpha$ -decay branches with energies and branching ratios [7261(5) keV, 53(2)%], [7235(5) keV, 30(2)%], and [7170(5) keV, 17(1)%] (see Fig. 3 in Ref. [27]).

In addition, the in-beam spectroscopy of  $^{221}\text{Ac}$  using the  $^{209}\text{Bi}(^{14}\text{C}, 2n)^{221}\text{Ac}$  reaction has been performed and a level scheme based on two alternating parity bands has been reported [30]. A tentative  $I^\pi = (3/2)^-$  ground state has been assigned, but the excited states obtained during this study do not match with the ones populated through  $\alpha$ -decay studies.

### B. $^{221}\text{Ac} \rightarrow ^{217}\text{Fr}$ $\alpha$ decay

As mentioned above, there is a disagreement on the spin assignment of the ground state of  $^{221}\text{Ac}$  between the in-beam [30] and  $\alpha$ -decay [24] experiments. The  $\alpha$  decay of  $^{221}\text{Ac}$  has been studied several times in the past [24–27,29],

TABLE I.  $\alpha$ -decay energies  $E_\alpha$ , branching ratios  $I_\alpha$ , hindrance factors (HF), and excitation energy of the populated states  $E_{\text{pop}}$  for  $^{225}\text{Pa} \rightarrow ^{221}\text{Ac}$  and for  $^{221}\text{Ac} \rightarrow ^{217}\text{Fr}$  taken from Ref. [24]. Those shown in square brackets are tentative.

Parent nuclei	$E_\alpha$ (keV)	$I_\alpha$ (%)	HF	$E_{\text{pop}}$ (keV)
$^{225}\text{Pa}(5/2^-)$	7264(3)	61(6)	2.6(3)	0
	7234(4)	15(4)	8.1(19)	30(5)
	[7205(8)]	9(3)	11(5)	60(8)
	7182(8)	5(2)	16(7)	88.2(15)
	7135(8)	1.8(6)	32(11)	124.9(12)
	7112(8)	3.7(13)	12(5)	152.2(15)
$^{221}\text{Ac}(5/2^-)$	7084(8)	4.0(12)	9(3)	179.8(15)
	7642(3)	71(4)	5.3(5)	0
	7440(3)	20(2)	4.1(5)	208.7(11)
	7364(5)	9(2)	5.2(12)	276.0(10)

with the most recent one [24] reporting three  $\alpha$ -decay branches (see Table I) consistent with the previously measured ones, as well as three  $\gamma$  transitions measured in coincidence for the first time. In Ref. [26], an additional  $\alpha$  decay was reported with energy and intensity [7170(10) keV,  $\approx 2\%$ ]. The ground state spin and parity of  $^{217}\text{Fr}$  was determined without ambiguity to be  $I^\pi = 9/2^-$ , due to a dominant unhindered  $\alpha$  decay towards the  $I^\pi = 9/2^-$  ground state of  $^{213}\text{At}$ . A tentative spin and parity assignment  $I^\pi = (5/2)^-$  for the first excited state and  $I^\pi = (7/2)^-$  for the second excited state have also been proposed [24].

### III. EXPERIMENTAL SETUP

Data presented in this article have been obtained during an experiment performed in July 2020 at the Ion Guide Isotope Separation On-Line (IGISOL) facility [31,32], University of Jyväskylä, Finland. The experimental setup is shown in Fig. 1. Neutron-deficient actinide nuclei were produced through proton-induced fusion-evaporation reactions with a 65-MeV primary beam (intensity between 1 and 3  $\mu\text{A}$ ) impinging on a  $^{232}\text{Th}$  target (2.2 mg/cm<sup>2</sup>). The reaction products exit the target thanks to the reaction kinematics and are stopped in the IGISOL light-ion guide, a small volume ( $\approx 1$  cm<sup>3</sup>) helium-filled gas cell ( $\approx 120$  mbar). They are then extracted and injected into the IGISOL beam line through a radiofrequency sextupole ion guide and finally mass separated by means of a dipole magnet ( $M/\Delta M \approx 500$ ) before being delivered to the decay station. The mass-selected nuclei are implanted into a 19  $\mu\text{g}/\text{cm}^2$  thick carbon foil surrounded by silicon and germanium detectors. Two 1-mm thick quadrant silicon detectors, composed of four pads of 24.75-mm width each, are placed either side of the foil, one at a distance of 26.7 mm from the foil and the other at 30.2 mm. One 500- $\mu\text{m}$  thick circular silicon detector ( $\approx 300$  mm<sup>2</sup> active area) is placed beneath the foil at a distance of 30.2 mm. Finally, a 4-mm thick liquid nitrogen cooled silicon-lithium [Si(Li)] detector ( $\approx 300$  mm<sup>2</sup> active area) is placed 20.6 mm behind the foil on the beam axis. The Si(Li) detector allowed the measurement of both  $\alpha$  particles ( $\approx 25$  keV FWHM energy resolution at 7 MeV) and conversion electrons ( $\approx 2$  keV FWHM energy resolution

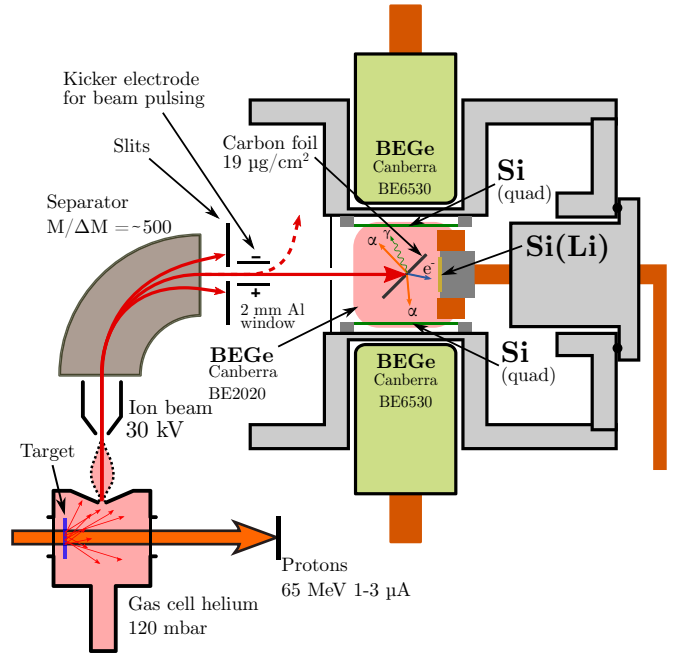


FIG. 1. Schematic view of the experimental setup (see text for details). The circular Si detector placed beneath the carbon foil and the BEGe detector placed above are not shown.

at 100 keV). The other silicon detectors measured only  $\alpha$  particles (between 30 and 40 keV FWHM energy resolution at 7 MeV). Four germanium detectors (BEGe) were also placed in a compact geometry around the chamber for the measurement of  $\gamma$  rays ( $\approx 1$  keV FWHM energy resolution at 300 keV).

The signals from the different detectors were recorded by mean of a triggerless data acquisition system composed of two NUTAQ VHS-ADC V4 14bit 100 MHz cards, synchronized by an external pulse. Each signal is processed by the board's internal FPGA using a moving window deconvolution filter to extract energy information and to time stamp the events that are sent to an acquisition computer where they are time sorted and written to disk. Data were then converted and analyzed using the ROOT [33] software.

## IV. EXPERIMENTAL RESULTS

### A. General considerations

$\alpha$ -particle energy calibrations were performed using on-line data (using the tabulated  $\alpha$ -decay energies of  $^{225}\text{Th}$  and  $^{226}\text{Th}$ , as well as  $^{221}\text{Ac}$  [34–37]) to take into account energy loss in the implantation foil. Electron energy calibrations were also performed with in-beam data, using  $\alpha$ -electron coincidences to clearly identify electron peaks originating from the  $^{225}\text{Th}$   $\alpha$  decay.  $\alpha$ -particle and electron detection efficiency calibrations were performed using a  $^{223}\text{Ra}$  source deposited on the tip of a needle placed at the central position of the implantation foil. The energy and efficiency calibrations of the germanium detectors was performed using  $^{133}\text{Ba}$  and  $^{152}\text{Eu}$  sources. A total detection efficiency of  $30.7 \pm 0.9\%$  is reached for the  $\alpha$ -particles and  $1.08 \pm 0.06\%$  for the electrons. A

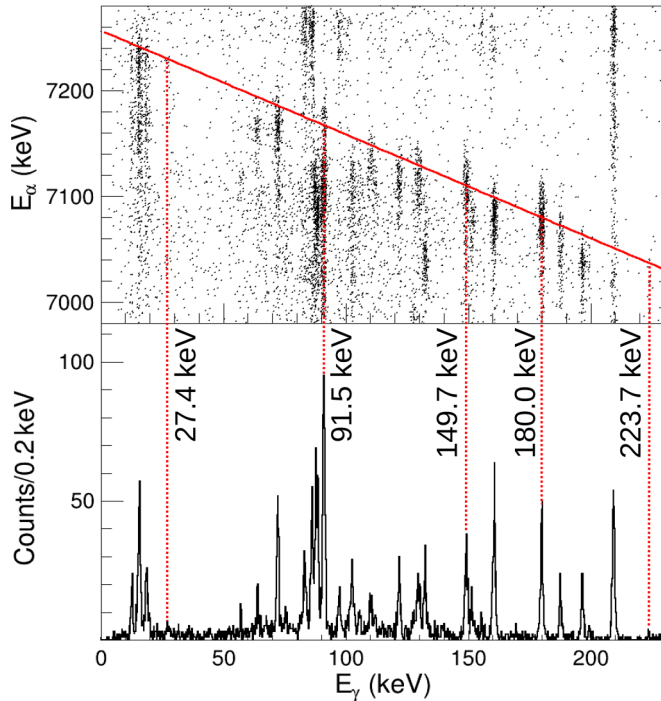


FIG. 2. Top:  $\alpha$ -particle energy ( $E_\alpha$ ) vs  $\gamma$ -ray energy ( $E_\gamma$ ) for  $^{225}\text{Pa} \rightarrow ^{221}\text{Ac}$ . The solid red line denotes the  $Q_\alpha + E_\gamma = Q_\alpha(\text{g.s.-to-g.s.})$  line where the coincidences with  $\gamma$  rays feeding directly the ground state are expected. Bottom: Projection of the top view on the  $x$  axis ( $E_\gamma$ ). The dashed red lines denote  $\alpha$ - $\gamma$  coincidences for which  $Q_\alpha + E_\gamma$  is close to  $Q_\alpha(\text{g.s.-to-g.s.})$ , linking them to the corresponding peak on the  $\gamma$ -energy spectrum. The associated  $\gamma$ -ray energy is indicated.

maximal  $\gamma$ -ray detection efficiency of  $16.5 \pm 1.0\%$  is reached at 105 keV.

Due to the implantation in a foil instead of directly in a silicon detector, summing of  $\alpha$  particles and conversion electrons can be neglected. However, during the  $\alpha$  decay, the recoil energy of the daughter nucleus is sufficient to release the daughter from the foil with  $\approx 50\%$  probability, leading to an unknown spatial distribution of daughter nuclei in the vacuum chamber. Indeed, the kinetic energy of the incoming ions is  $\approx 30$  keV, whereas the recoil energy is of the order of 100 keV during  $\alpha$  decay. Thus, the  $\alpha$ -particle energy calibration needs to be adjusted for the daughter nuclei to take into account the different energy losses of the  $\alpha$  particle before reaching the detectors. In addition, efficiency calibrations cannot be applied to the decay of the daughter nuclei as their spatial distribution within the experimental chamber is not known.

Identification of  $\alpha$  particles emitted by a given nucleus is performed through  $\alpha$ - $\gamma$  coincidences, measuring the sum of  $Q_\alpha + E_\gamma$  and its vicinity (within  $\pm 3$  keV) to the ground state-to-ground state energy [ $Q_\alpha(\text{g.s.-to-g.s.})$ ] as shown in Fig. 2.  $E_\gamma$  is the measured  $\gamma$ -ray energy while  $Q_\alpha$  values are calculated using the  $\alpha$ -particle energy  $E_\alpha$  and the equation  $Q_\alpha = \frac{m_d + m_\alpha}{m_d} \times E_\alpha$ , with  $m_\alpha$  the mass of the  $\alpha$  particle and  $m_d$  the mass of the daughter nucleus. To extract  $\alpha$ -decay energies and intensities, a fit of the whole  $\alpha$ -energy spectrum is done using a sum of deformed gaussian functions (one for

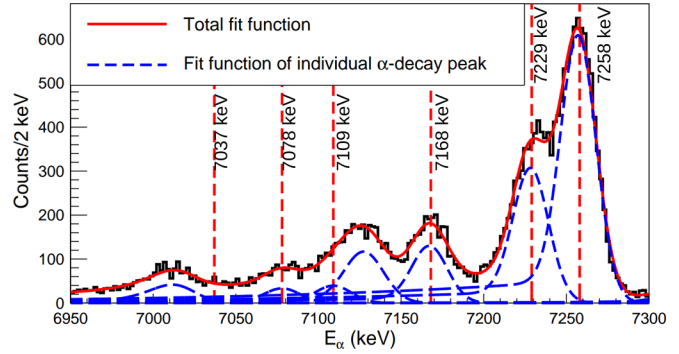


FIG. 3.  $\alpha$ -energy spectrum ( $E_\alpha$ ) in the Si(Li) between 6.95 MeV and 7.3 MeV, corresponding to the  $\alpha$ -decay energy region of  $^{225}\text{Pa}$ . The total fit can be seen as a solid red line and each peak contribution can be seen as blue dashed lines. Vertical dashed lines indicate  $^{225}\text{Pa}$   $\alpha$  decay with the measured  $E_\alpha$  highlighted. The two  $\alpha$  peaks that are not denoted with the vertical lines are contamination coming from  $^{222}\text{Ac}$  (7008.6 keV,  $^{226}\text{Pa}$  decay chain) and  $^{218}\text{Rn}$  (7129.1 keV,  $^{226}\text{Th}$  decay chain).

each peak) and with no background. Each deformed gaussian function is defined as

$$S(E) = I \times \left[ \frac{p}{\sqrt{2\pi}\sigma} e^{-\frac{(E-\mu)^2}{2\sigma^2}} + \frac{(1-p)\beta e^{-\frac{\beta^2}{4} + \beta \frac{E-\mu}{\sigma}} (1 + \text{erf}(\frac{-(E-\mu)}{\sigma}))}{2\sigma} \right]$$

with  $I$  the integral of the function,  $\mu$  the centroid,  $\sigma$  the standard deviation,  $\beta$  the deformation parameter,  $p$  a weighting factor between the deformed part and the gaussian part, and erf the error function.

A zoom of the region between 6.95 MeV and 7.3 MeV is presented in Fig. 3. The gaussian function form parameters ( $\sigma$ ,  $p$ , and  $\beta$ ) are forced to have the same value for all  $\alpha$ -decay peaks at a given position in the decay chain. Indeed the shape of  $\alpha$  peaks for nuclei directly implanted in the foil should be the same. However, since part of the decay of the daughter nuclei occurs outside of the foil, the material seen by the  $\alpha$  particle before detection is different, resulting in energy loss and straggling changes and thus modifying the shape of the peak. This allowed the fit of the whole  $\alpha$ -energy spectrum with a reduced number of parameters.

Using the  $Q_\alpha + E_\gamma = Q_\alpha(\text{g.s.-to-g.s.})$  line shown in Fig. 2, the  $\gamma$  rays directly feeding the ground state can be identified and thus the energy levels can be determined. The remaining  $\gamma$  rays are then placed within the level scheme using  $\alpha$ - $\gamma$  coincidences and levels energy differences.

The BrIcc (band-Raman internal conversion coefficients) code [38] is used to compute expected conversion electron energies and coefficients for each transition. The conversion coefficients obtained for each multipolarity are then compared with the measured ones. Due to a very low electron detection efficiency ( $\approx 1\%$ ), no electrons are detected at the expected energy in most cases. In this case, an upper limit is set on the number of emitted electrons and thus on the conversion coefficient with a confidence interval of 95%. In most cases

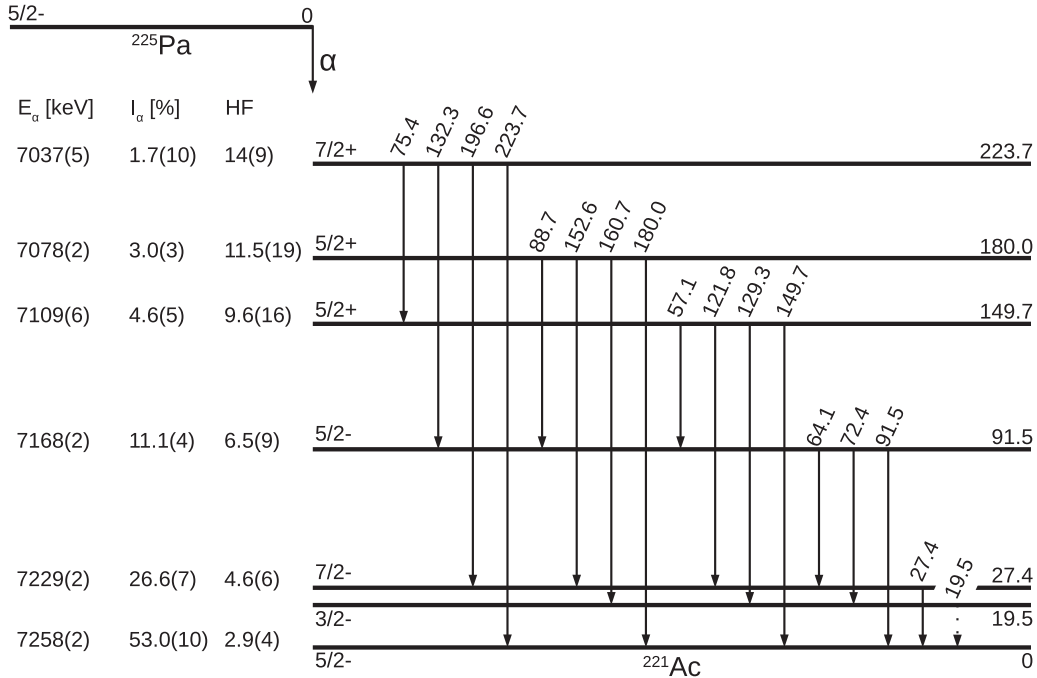


FIG. 4. Deduced decay scheme for  $^{225}\text{Pa} \rightarrow ^{221}\text{Ac}$   $\alpha$  decay. The  $\alpha$ -particle energies  $E_\alpha$ , intensities  $I_\alpha$ , and hindrance factors (HF) are given, as well as the levels,  $\gamma$ -transition energies, and the proposed spin-parity assignment.

this upper limit, combined with parity-based considerations, allows the multipolarity of the transition to be determined.

### B. $A = 225$

Approximately 12 h of data acquisition was obtained for mass  $A = 225$ . The  $\alpha$ -energy spectrum displays several contributions. The two main contributions are from  $^{225}\text{Th}$  and  $^{225}\text{Pa}$  and their respective  $\alpha$ -decay chains. In addition, there is a contribution coming from the  $\alpha$ -decay chains of  $^{226}\text{Th}$  and  $^{226}\text{Pa}$  as both are partly transmitted through the mass separator. Finally, the implantation foil has a remaining contamination of long-lived  $^{224}\text{Ra}$  ( $T_{1/2} \approx 3.6$  d) and  $^{223}\text{Ra}$  ( $T_{1/2} \approx 11.4$  d) originating from a previous run selecting mass  $A = 224$  and from the  $^{223}\text{Ra}$  calibration source. A fit of the whole  $\alpha$ -energy spectrum using a sum of deformed gaussian functions (Fig. 3) is performed in order to extract each peak centroid and intensity with one exception: The 7037-keV  $\alpha$  decay. This transition is at the limit of our detection capabilities and its intensity cannot be determined directly from the  $\alpha$ -energy spectrum. It was determined using  $\alpha$ - $\gamma$  coincidences and thus has a larger relative uncertainty as the detection efficiencies are taken into account. The  $\alpha$ -decay hindrance factors for  $^{225}\text{Pa}$  decay are extracted from the energies and intensities using Preston's spin-independent equations [39,40] with  $r_0 = 1.5475$  fm interpolated from neighboring even-even nuclei and  $T_{1/2} = 1.95(10)$  s the lifetime measured in Ref. [24]. The  $\alpha$ - $\gamma$  coincidence two-dimensional energy spectrum and its projection on the  $x$  axis ( $E_\gamma$ ) is shown in Fig. 2. The results are summarised in Fig. 4 and compared with results from Ref. [24] in Table III. The measured  $\gamma$ -transition energies, intensities, and multipolarities are reported in Table II.

The 19.5-keV level is proposed as it is fed by three different  $\gamma$  transitions ( $[E_i = 91.5$  keV,  $E_\gamma = 72.4$  keV],  $[E_i = 149.7$

TABLE II. Measured  $\gamma$ -ray energies  $E_\gamma$ , initial level energies  $E_i$ , intensities  $I_\gamma$  (number of  $\gamma$  emitted for 100  $\alpha$  decays), and multipolarity assignments. Multipolarities deduced using parity arguments are denoted with a star.

Nucleus	$E_i$ (keV)	$E_\gamma$ (keV)	$I_\gamma$	Multipolarities		
$^{221}\text{Ac}$	223.7	223.7(5)	0.044(13)	?		
		196.6(1)	0.34(5)	$E1^*$		
		132.3(3)	0.37(5)	$E1$		
		75.4(2)	0.048(16)	$M1^*$		
		180.0	180.0(1)	0.74(10)	$E1$	
			160.7(1)	0.72(9)	$E1$	
			152.6(2)	0.21(4)	$E1^*$	
			88.7(3)	0.43(6)	$E1$	
			149.7(3)	0.52(7)	$E1^*$	
		149.7	129.3(3)	0.34(5)	$E1$	
			121.8(1)	0.31(4)	$E1$	
			57.1(1)	0.066(23)	$E1^*$	
			91.5	91.5(2)	0.43(10)	$M1 + E2$ or $E2$
				72.4(1)	0.48(6)	$M1 + E2$
64.1(1)	0.148(25)	$M1 + E2$ or $M1$				
$^{217}\text{Fr}$	27.4	27.4(1)	0.032(16)	$M1 + E2$ or $M1$		
		579.0	579.0(10)			
			87.8(2)			
			491.8	491.8(1)		
				283.0(10)		
			364.7	364.7(1)		
				155.6(1)		
			275.7	275.7(1)		
				44.3(1)		
			231.4	231.4(1)		
209.4	209.4(1)					
	98.8	98.8(14)				

TABLE III. Comparison between Ref. [24] and this work for  $\alpha$ -decay energies  $E_\alpha$ , branching ratios  $I_\alpha$ , hindrance factors (HF), and excitation energy of the populated states  $E_{\text{pop}}$  for  $^{225}\text{Pa} \rightarrow ^{221}\text{Ac}$ . Those shown in square brackets are tentative.

Parent nuclei	Ref. [24]				This work			
	$E_\alpha$ (keV)	$I_\alpha$ (%)	HF	$E_{\text{pop}}$ (keV)	$E_\alpha$ (keV)	$I_\alpha$ (%)	HF	$E_{\text{pop}}$ (keV)
$^{225}\text{Pa}(5/2^-)$	7264(3)	61(6)	2.6(3)	0	7258(2)	53.0(10)	2.9(4)	0
	7234(4)	15(4)	8.1(19)	30(5)	7229(2)	26.6(7)	4.6(6)	27.4(1)
	[7205(8)]	9(3)	11(5)	60(8)				
	7182(8)	5(2)	16(7)	88.2(15)	7168(2)	11.1(4)	6.5(9)	91.5(2)
	7135(8)	1.8(6)	32(11)	124.9(12)				
	7112(8)	3.7(13)	12(5)	152.2(15)	7109(6)	4.6(5)	9.6(16)	149.7(3)
	7084(8)	4.0(12)	9(3)	179.8(15)	7078(2)	3.0(3)	11.5(19)	180.0(1)
					7037(5)	1.7(10)	14(9)	223.7(5)

keV,  $E_\gamma = 129.3$  keV], [ $E_i = 180.0$  keV,  $E_\gamma = 160.7$  keV]). However, the  $\gamma$  transition from this level to  $^{221}\text{Ac}$  ground state is not clearly observed as it is mixed with x rays close in energy, and no  $\alpha$  decay toward this level is observed. For all other levels in the decay scheme, the  $Q_\alpha + E_\gamma$  values are consistent and enables an improvement of the uncertainty on the g.s.-to-g.s.  $Q_\alpha$  value:  $Q_\alpha(\text{g.s.-to-g.s.}) = 7388 \pm 1$  keV, compared to the previous value  $Q_\alpha(\text{g.s.-to-g.s.}) = 7380 \pm 50$  keV [34].

The  $\alpha$ - $\gamma$  coincidences seen in this study are not fully in agreement with the results presented in Ref. [24] (cf Table III). Notably, two  $\alpha$  branches,  $E_\alpha = 7205$  keV and  $E_\alpha = 7135$  keV are not seen in this work. The  $E_\alpha = 7205$  keV  $\alpha$  transition is only proposed tentatively in Ref. [24]. The  $E_\alpha = 7135$  keV  $\alpha$  transition is seen in Ref. [24] in coincidence with a  $\gamma$  ray of energy  $E_\gamma = 125$  keV, extracted from a statistics of 3  $\alpha$ - $\gamma$  counts. In the present work no  $\gamma$  rays are seen coming out of the background between the  $\gamma$  rays with  $E_\gamma = 121.8$  keV and  $E_\gamma = 129.3$  keV, whereas the  $E_\gamma = 125$  keV line is the strongest transition seen in Ref. [24]. In addition, although an  $\alpha$  decay is seen around  $E_\alpha = 7135$  keV, in the present work it is clearly identified as a contamination from the  $\alpha$  decay of  $^{218}\text{Rn}$  coming from the  $^{226}\text{Th}$  decay chain. Finally, the  $E_\alpha = 7037$  keV  $\alpha$  transition seen in the present work is not reported in Ref. [24]. This  $\alpha$  branch is very weak compared to the other branches and the  $\gamma$  ray feeding directly the ground state has a low branching ratio, making the transition hard to identify with low statistics.

It should be noted that, for the 149.7-keV level, the total de-excitation intensity [ $I_{\text{tot}} = 1.55(12)\%$ ] is significantly lower than the  $\alpha$  branching ratio feeding this state [ $I_\alpha = 4.6(5)\%$ ]. A possible explanation for this is given in the discussion section.

The 27.4-keV transition is tentatively assigned as an  $M1 + E2$  on the basis of the ratio between the number of emitted  $\gamma$  rays and  $\alpha$  particles (assuming no transition from this level to the 19.5 keV level). This ratio indicates a conversion coefficient  $\alpha_e \approx 1000$  that lies between the predictions for  $M1$  ( $\alpha_e = 152.8$ ) and  $E2$  ( $\alpha_e = 5380$ ) transitions. However, the large uncertainty on the BEGe detection efficiency at this energy, as well as the assumption that there is no competing transition, could reduce considerably this conversion coefficient, making it potentially consistent with a pure  $M1$  transition.

For several transitions, conversion coefficients are not sufficient to determine the multipolarity, however in all cases but one the ambiguity on the multipolarity can be resolved on the basis of the parity of the initial and final states. See the Appendix for the detail of the multipolarity assignments.

### C. $A = 221$

Approximately 2 h of data acquisition was obtained for mass  $A = 221$ . In order to collect more statistics, data for mass  $A = 225$  were also used in the analysis. The measured  $\alpha$  decays are reported in Fig. 5, the measured  $\gamma$  rays in Table II and the spectra are presented in Fig. 6. Since, as detailed above, the recoil energy of the daughter nucleus is large enough for it to escape from the implantation foil, the detection efficiencies

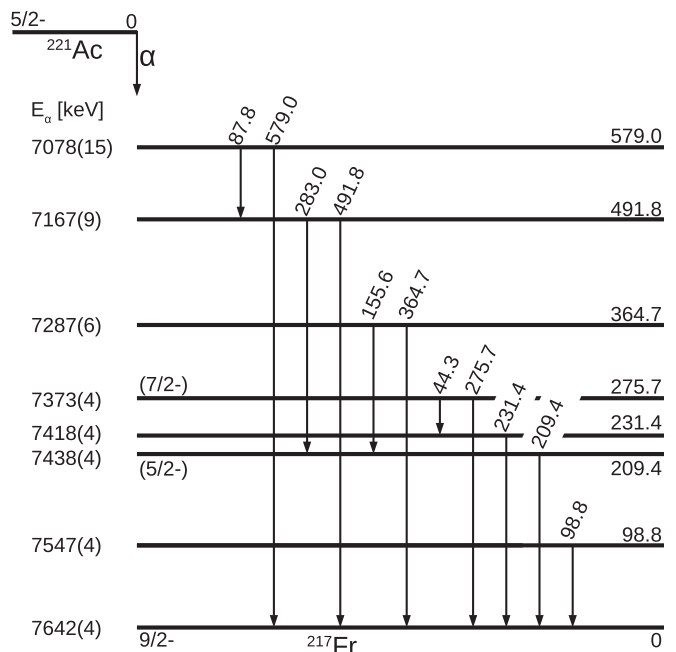


FIG. 5. Measured decay scheme for  $^{221}\text{Ac} \rightarrow ^{217}\text{Fr}$   $\alpha$  decay. The  $\alpha$ -particle energies  $E_\alpha$ , the  $\gamma$ -transition energies  $E_\gamma$ , as well as the proposed spin-parity assignment and energies of the levels are presented.

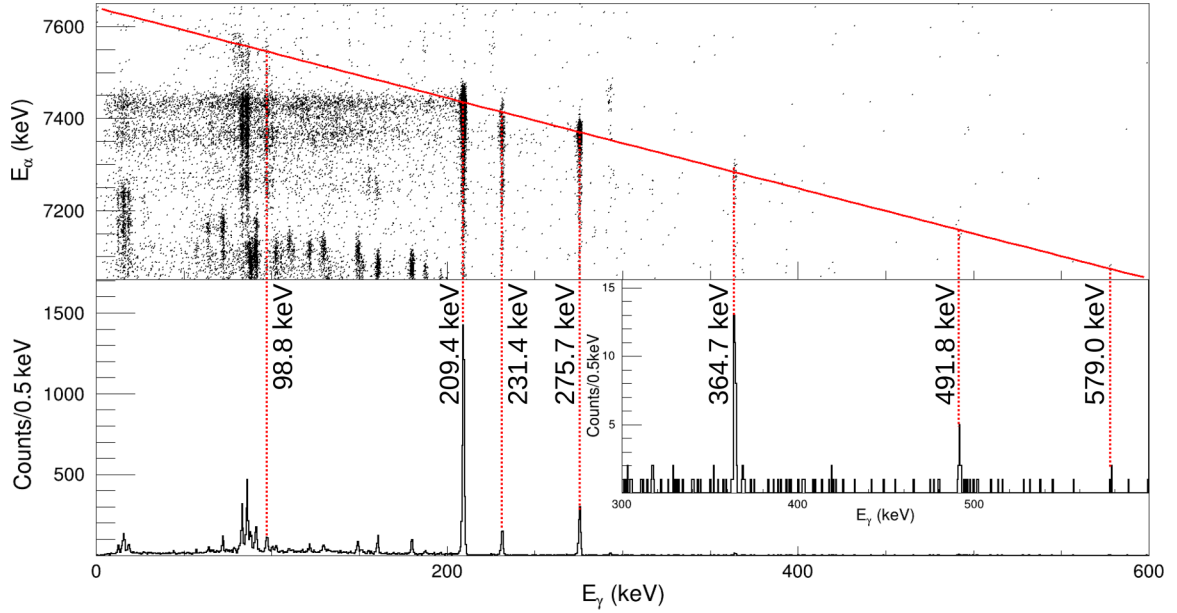


FIG. 6. Top:  $\alpha$ -particle energy ( $E_\alpha$ ) vs  $\gamma$ -ray energy ( $E_\gamma$ ) for  $^{221}\text{Ac} \rightarrow ^{217}\text{Fr}$ . The solid red line denotes the  $Q_\alpha + E_\gamma = Q_\alpha(\text{g.s.-to-g.s.})$  line where the coincidences with  $\gamma$  ray feeding directly the ground state are expected. Bottom: Projection of the top view on the  $x$  axis ( $E_\gamma$ ), as well as a zoom for the 300–600-keV energy region in the inset. The dashed red lines denotes  $\alpha$ - $\gamma$  coincidences for which  $Q_\alpha + E_\gamma$  is close to  $Q_\alpha(\text{g.s.-to-g.s.})$ , linking them to the corresponding peak on the  $\gamma$ -energy spectrum. The associated  $\gamma$ -ray energy is indicated.

are not available for the decay of  $^{221}\text{Ac} \rightarrow ^{217}\text{Fr}$  as the spatial distribution of  $^{221}\text{Ac}$  is unknown. In this paper, only the observed  $\alpha$ -decay and  $\gamma$ -ray energies are reported.

All  $Q_\alpha + E_\gamma$  values are fully consistent with each other within error bars and enables an improvement of the uncertainty on the g.s.-to-g.s.  $Q_\alpha$  value:  $Q_\alpha(\text{g.s.-to-g.s.}) = 7785 \pm 2$  keV, compared to the previous value  $Q_\alpha(\text{g.s.-to-g.s.}) = 7780 \pm 50$  keV [34]. The transition  $E_\gamma = 364.7$  keV matches one of the transitions ( $E_\gamma = 364$  keV) observed in a high-spin study in Ref. [41].

In the data for mass  $A = 225$ , two  $\alpha$  decays (at  $E_\alpha = 7078$  keV and  $E_\alpha = 7168$  keV) are observed in coincidence with several  $\gamma$  rays, in part being consistent with an assignment to the  $\alpha$  decay from  $^{225}\text{Pa}$  to  $^{221}\text{Ac}$  while others with an assignment to the  $\alpha$  decay from  $^{221}\text{Ac}$  to  $^{217}\text{Fr}$ . The data suggest that both  $^{225}\text{Pa}$  and  $^{221}\text{Ac}$  emit  $\alpha$  particles at approximately the same energy, however, further experiments are needed to confirm this.

## V. DISCUSSION

An extensive discussion of the ground-state configurations of odd- $A$  actinium and protactinium isotopes is given in Ref. [24], leading to a  $I^\pi = 5/2^-$  assignment for both  $^{225}\text{Pa}$  and  $^{221}\text{Ac}$ . Our results are consistent with this assignment and are summarized hereafter.

A similarity is found between the  $\alpha$  decay of  $^{227}\text{Pa}$  reported in Ref. [20] and the  $\alpha$  decay of  $^{225}\text{Pa}$  reported here (Fig. 7). In both cases, the lowest hindrance factor is observed for the decay toward the ground state with very similar values. This is consistent with microscopic-macroscopic calculations that break the reflection symmetry [4]. Indeed, those calculations

predict two orbitals ( $\Omega = 3/2$  and  $\Omega = 5/2$ ) present around the proton Fermi level for both Ac ( $Z = 89$ ) and Pa ( $Z = 91$ ) isotopes with  $N \approx 130$ –140 [4,6,7]. For a quadrupole deformation above  $\epsilon \approx 0.1$ , the  $\Omega = 3/2$  orbital is the lowest energy orbital and should be the ground state of Ac isotopes, while the  $\Omega = 5/2$  orbitals should be the ground state of Pa isotopes. However, as the quadrupole deformation decreases, the two orbitals cross, hence the  $\Omega = 5/2$  becomes the lowest energy one. The  $^{227}\text{Pa}$  and  $^{225}\text{Pa}$  are expected to have a larger quadrupole deformation than their daughter Ac isotopes. Thus, the  $\Omega = 5/2$  orbital would be the ground state of all four nuclei ( $^{227}\text{Pa}$ ,  $^{223}\text{Ac}$ ,  $^{225}\text{Pa}$ , and  $^{221}\text{Ac}$ ), which explains the very low hindrance factor toward the ground state in both cases.

In addition, similar hindrance factors are also observed toward the excited states, with notably low hindrance factors ( $\text{HF} \approx 10$ ) toward opposite parity states. This kind of behavior has been interpreted several times as a sign of octupole deformation where opposite parity states mix and lead to low hindrance factors for transitions toward opposite parity states [20–23].

Considering the similarity between the  $^{221}\text{Ac}$  and  $^{223}\text{Ac}$  level schemes, the  $I^\pi = 3/2^+$  state at 88.9 keV in  $^{223}\text{Ac}$  is also expected in  $^{221}\text{Ac}$ . The presence of this unobserved state could explain the missing intensity from the 149.7-keV state in  $^{221}\text{Ac}$ . With a hindrance factor of  $\approx 100$  for this  $3/2^+$  state in  $^{223}\text{Ac}$ , it is not surprising that it is not observed in this study.

Finally, the  $I^\pi = 5/2^-$  and  $I^\pi = 5/2^+$  levels could be interpreted as a parity doublet arising from octupole deformation. The splitting of 149.7 keV for the doublet seems higher than the splitting usually reported in the literature

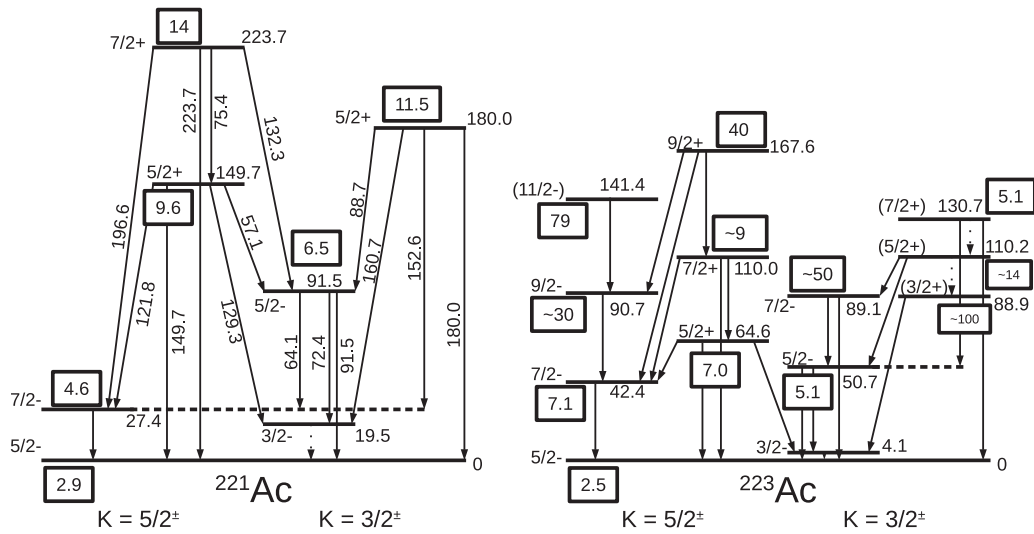


FIG. 7. Comparison between the proposed level scheme interpretation for  $^{221}\text{Ac}$  and the level scheme of  $^{223}\text{Ac}$ . The numbers in the black boxes are the hindrance factors of the  $\alpha$  decay feeding those states. Data for  $^{223}\text{Ac}$  are taken from Ref. [20].

[20,23,42–45]. However, it is also smaller than the one reported for  $^{219}\text{Fr}$ , which is considered as a transitional nucleus between static octupole deformation and octupole vibration with a splitting of 191.4 keV for the ground-state band [46]. Thus  $^{221}\text{Ac}$  could be interpreted as the onset of the transitional region between static octupole deformation and octupole vibration for the Ac isotopes. This interpretation is consistent with the results presented in Ref. [47] where self-consistent blocked Hartree-Fock-Bogoliubov calculations using the energy density functional SLy5s1 provides the best agreement with the data and predicts the static octupole deformation to occur between  $N = 130$  and  $N = 142$  for Ac isotopes.

## VI. SUMMARY

The low-lying excitation schemes of  $^{221}\text{Ac}$  and  $^{217}\text{Fr}$  have been studied at the IGISOL facility, University of Jyväskylä, via the  $\alpha$ -decay chain  $^{225}\text{Pa} \rightarrow ^{221}\text{Ac} \rightarrow ^{217}\text{Fr}$ . The nuclei of interest were produced using a proton-induced fusion-evaporation reaction on a  $^{232}\text{Th}$  target. The level scheme of  $^{221}\text{Ac}$  is interpreted in terms of parity-doublet bands arising from a static reflection asymmetric shape, and is compared with the level scheme of  $^{223}\text{Ac}$ . This, added with the need to include reflection asymmetry in the Nilsson orbitals to understand the band heads and the low hindrance factor toward opposite parity states seems to indicate the presence of a static

TABLE IV. Measured conversion coefficient  $\alpha_K$ ,  $\alpha_L$ , and/or  $\alpha_M$ , BrIcc conversion coefficients, and deduced multipolarity assignments for each  $\gamma$  transition seen in  $^{221}\text{Ac}$  where conversion coefficients could be computed. Upper limits on conversion coefficients are given with a 95% confidence interval. When a transition is potentially a mixed transition, the computed mixing coefficient  $\delta$  is also given. Assignments denoted with a star are deduced partially using parity arguments.

Transition energy (keV)	Measurement	BrIcc			Assignment
		$E1$	$M1$	$E2$	
64.1	$\alpha_L = 30.2 \pm 7.3$	0.3	9.5	62.6	$M1 + E2$ or $M1$
	$\alpha_M = 3.8 \pm 1.6$	0.07	2.27	17.1	$\delta = 0.5 \pm 0.1$
	$\alpha_L = 11.8 \pm 1.9$	0.2	6.6	34.9	$M1 + E2$
72.4	$\alpha_M = 7.0 \pm 1.7$	0.05	1.6	9.6	$\delta = 0.4 \pm 0.1$
	$\alpha_M < 0.73$	0.03	0.9	3.7	$E1$
	$\alpha_L = 13.6 \pm 3.6$	0.1	3.3	11.5	$M1 + E2$ or $E2$
91.5	$\alpha_M = 1.9 \pm 1.1$	0.03	0.8	3.15	$\delta = 1.3 \pm 0.2$
	$\alpha_L < 0.86$	0.05	1.5	3.1	$E1$
	$\alpha_L < 0.72$	0.04	1.2	2.4	$E1$
129.3	$\alpha_L < 0.47$	0.04	1.2	2.1	$E1$
	$\alpha_M < 0.47$	0.01	0.3	0.6	$E1$
	$\alpha_L < 1$	0.03	0.8	1.2	$E1^*$
149.7	$\alpha_L < 0.27$	0.03	0.7	0.9	$E1$
	$\alpha_M < 0.17$	0.006	0.2	0.2	$E1$
	$\alpha_L < 0.16$	0.02	0.5	0.5	$E1$
180.1	$\alpha_K < 0.69$	0.08	2	0.2	$E1^*$

octupole deformation in  $^{221}\text{Ac}$ , in coherence with some recent calculations. These results suggest that  $^{221}\text{Ac}$  represents a transitional nucleus between static octupole deformation and octupole vibration. It would be important to continue this work with the study of the  $\alpha$  decay of  $^{223}\text{Pa}$  to  $^{219}\text{Ac}$  to confirm that  $^{221}\text{Ac}$  lies at the boundary of the region of octupole deformation for the actinium isotopes.

The use of implantation foils in  $\alpha$ -decay experiments provide complementary information compared to recoil decay tagging experiments, notably through the measurement of conversion electron energy and  $\alpha$ -electron coincidences. In the future, such experiments can be coupled with laser spectroscopy to obtain ground-state properties. Indeed, the coupling of decay spectroscopy and laser spectroscopy could provide a powerful experimental approach to pin down the structure of these neutron-deficient actinides.

## ACKNOWLEDGMENTS

This work is supported in part by the Institut Français de Finlande, the Embassy of France in Finland, the French Ministry of Higher Education, Research and Innovation, the Finnish Society of Sciences and Letters and the Finnish Academy of Science and Letters. This project has also received funding from the Academy of Finland under Project No. 339245, and from the European Union's Horizon 2020 research and innovation programme under Grant Agreement No. 861198-LISA-H2020-MSCA-ITN-2019 and Grant Agreement No. 771036 (ERC CoG MAIDEN).

## APPENDIX: CONVERSION COEFFICIENTS AND MULTIPOLARITIES

Details of the multipolarity assignments are found in Table IV.

- 
- [1] I. Ahmad and P. A. Butler, Octupole shapes in nuclei, *Annu. Rev. Nucl. Part. Sci.* **43**, 71 (1993).
- [2] P. A. Butler and W. Nazarewicz, Intrinsic reflection asymmetry in atomic nuclei, *Rev. Mod. Phys.* **68**, 349 (1996).
- [3] P. A. Butler, Octupole collectivity in nuclei, *J. Phys. G: Nucl. Part. Phys.* **43**, 073002 (2016).
- [4] G. A. Leander and R. K. Sheline, Intrinsic reflection asymmetry in odd-A nuclei, *Nucl. Phys. A* **413**, 375 (1984).
- [5] R. K. Sheline, Definition of the actinide region of static quadrupole-octupole deformation, *Phys. Lett. B* **197**, 500 (1987).
- [6] G. A. Leander and Y. S. Chen, Reflection-asymmetric rotor model of odd A  $\sim 219$ – $229$  nuclei, *Phys. Rev. C* **37**, 2744 (1988).
- [7] S. Cwiok and W. Nazarewicz, Reflection-asymmetric shapes in odd-A actinide nuclei, *Nucl. Phys. A* **529**, 95 (1991).
- [8] L. M. Robledo and R. R. Rodríguez-Guzmán, Octupole deformation properties of actinide isotopes within a mean-field approach, *J. Phys. G: Nucl. Part. Phys.* **39**, 105103 (2012).
- [9] L. P. Gaffney *et al.*, Studies of pear-shaped nuclei using accelerated radioactive beams, *Nature (London)* **497**, 199 (2013).
- [10] S. E. Agbemava, A. V. Afanasjev, and P. Ring, Octupole deformation in the ground states of even-even nuclei: A global analysis within the covariant density functional theory, *Phys. Rev. C* **93**, 044304 (2016).
- [11] S. E. Agbemava and A. V. Afanasjev, Octupole deformation in the ground states of even-even  $z \sim 96$ ,  $n \sim 196$  actinides and superheavy nuclei, *Phys. Rev. C* **96**, 024301 (2017).
- [12] Y. Cao, S. E. Agbemava, A. V. Afanasjev, W. Nazarewicz, and E. Olsen, Landscape of pear-shaped even-even nuclei, *Phys. Rev. C* **102**, 024311 (2020).
- [13] H. Abusara, A. V. Afanasjev, and P. Ring, Fission barriers in covariant density functional theory: Extrapolation to superheavy nuclei, *Phys. Rev. C* **85**, 024314 (2012).
- [14] J.-F. Lemaître, S. Goriely, S. Hilaire, and N. Dubray, Microscopic description of the fission path with the Gogny interaction, *Phys. Rev. C* **98**, 024623 (2018).
- [15] M. Warda and L. M. Robledo, Microscopic description of cluster radioactivity in actinide nuclei, *Phys. Rev. C* **84**, 044608 (2011).
- [16] M. Warda, A. Zdeb, and L. M. Robledo, Cluster radioactivity in superheavy nuclei, *Phys. Rev. C* **98**, 041602(R) (2018).
- [17] J. Engel, M. Bender, J. Dobaczewski, J. H. de Jesus, and P. Olbratowski, Time-reversal violating schiff moment of  $^{225}\text{Ra}$ , *Phys. Rev. C* **68**, 025501 (2003).
- [18] V. V. Flambaum, Enhanced nuclear Schiff moment and time-reversal violation in  $^{229}\text{Th}$ -containing molecules, *Phys. Rev. C* **99**, 035501 (2019).
- [19] G. Arrowsmith-Kron *et al.*, Opportunities for fundamental physics research with radioactive molecules (2023), [arXiv:2302.02165](https://arxiv.org/abs/2302.02165).
- [20] R. K. Sheline, C. F. Liang, and P. Paris, Level structure and reflection asymmetric shape in  $^{223}\text{Ac}$ , *Int. J. Mod. Phys. A* **05**, 2821 (1990).
- [21] R. K. Sheline and BothoBo-Mbaka Bossinga, Alpha decay hindrance factors and reflection asymmetry in nuclei, *Phys. Rev. C* **44**, 218 (1991).
- [22] R. K. Sheline, Comment on the question of reflection asymmetry in  $^{229}\text{Pa}$ , *Phys. Rev. C* **48**, 1003 (1993).
- [23] R. K. Sheline, C. F. Liang, P. Paris, J. Kvasil, and D. Nosek, Experimental and theoretical study of the nuclear structure of  $^{223}\text{Fr}$ , *Phys. Rev. C* **51**, 1708 (1995).
- [24] E. Parr *et al.*, Single-particle states and parity doublets in odd-Z  $^{221}\text{Ac}$  and  $^{225}\text{Pa}$  from  $\alpha$ -decay spectroscopy, *Phys. Rev. C* **105**, 034303 (2022).
- [25] R. L. Hahn, M. F. Roche, and K. S. Toth, New neptunium isotopes,  $^{230}\text{Np}$  and  $^{229}\text{Np}$ , *Nucl. Phys. A* **113**, 206 (1968).
- [26] J. Borggreen, K. Valli, and E. K. Hyde, Production and decay properties of protactinium isotopes of mass 222 to 225 formed in heavy-ion reactions, *Phys. Rev. C* **2**, 1841 (1970).
- [27] M. Huyse, P. Dendooven, and K. Deneffe, Production and mass separation of short-living neutron-deficient actinides, *Nucl. Instrum. Methods Phys. Res. B* **31**, 483 (1988).
- [28] M. Sakama *et al.*, New isotope  $^{233}\text{Am}$ , *Eur. Phys. J. A* **9**, 303 (2000).
- [29] A. K. Mistry *et al.*, Decay spectroscopy of heavy isotopes at SHIP using the COMPASS focal plane detection set-up, *Acta Phys. Pol. B* **49**, 613 (2018).
- [30] M. Aïche *et al.*, High-spin spectroscopy of the reflection-asymmetric nucleus  $^{221}\text{Ac}$ , *Nucl. Phys. A* **567**, 685 (1994).

- [31] J. Äystö, Development and applications of the IGISOL technique, *Nucl. Phys. A* **693**, 477 (2001).
- [32] I. Moore *et al.*, Towards commissioning the new IGISOL-4 facility, *Nucl. Instrum. Methods Phys. Res. B* **317**, 208 (2013).
- [33] R. Brun and F. Rademakers, ROOT — An object oriented data analysis framework, *Nucl. Instrum. Methods Phys. Res. A* **389**, 81 (1997).
- [34] Y. A. Akovali, Nuclear data sheets for  $A = 221$ , *Nucl. Data Sheets* **61**, 623 (1990).
- [35] S. Singh, A. Jain, and J. K. Tuli, Nuclear data sheets for  $A = 222$ , *Nucl. Data Sheets* **112**, 2851 (2011).
- [36] F. Kondev *et al.*, Nuclear data sheets for  $A = 217$ , *Nucl. Data Sheets* **147**, 382 (2018).
- [37] B. Singh *et al.*, Nuclear data sheets for  $A = 219$ , *Nucl. Data Sheets* **175**, 150 (2021).
- [38] T. Kibédi, T. Burrows, M. Trzhaskovskaya, P. Davidson, and C. Nestor, Evaluation of theoretical conversion coefficients using BrIcc, *Nucl. Instrum. Methods Phys. Res. A* **589**, 202 (2008).
- [39] M. A. Preston, The theory of alpha-radioactivity, *Phys. Rev.* **71**, 865 (1947).
- [40] S. Singh, S. Kumar, B. Singh, and A. K. Jain, Nuclear radius parameters ( $r_0$ ) for even-even nuclei from alpha decay, *Nucl. Data Sheets* **167**, 1 (2020).
- [41] M. Aiche, A. Chevallier, J. Chevallier, S. Hulne, S. Khazrouni, N. Schulz, and J. C. Sens, Yrast states of  $^{217}\text{Fr}$  and the onset of static intrinsic reflection asymmetric shapes in the light actinide region, *J. Phys. G* **14**, 1191 (1988).
- [42] I. Ahmad, R. Holzmann, R. V. F. Janssens, P. Dendooven, M. Huyse, G. Reusen, J. Wauters, and P. Van Duppen, Octupole deformation in  $^{223}\text{Ac}$ , *Nucl. Phys. A* **505**, 257 (1989).
- [43] I. Ahmad, J. E. Gindler, R. R. Betts, R. R. Chasman, and A. M. Friedman, Possible Ground-State Octupole Deformation in  $^{229}\text{Pa}$ , *Phys. Rev. Lett.* **49**, 1758 (1982).
- [44] G. Ardisson, J. Gasparro, V. Barci, and R. K. Sheline, Levels in  $^{221}\text{Fr}$  fed by the  $\alpha$  decay of  $^{225}\text{Ac}$ , *Phys. Rev. C* **62**, 064306 (2000).
- [45] I. Ahmad, J. E. Gindler, A. M. Friedman, R. R. Chasman, and T. Ishii, Level structure of  $^{225}\text{Ac}$ , *Nucl. Phys. A* **472**, 285 (1987).
- [46] C. F. Liang, P. Paris, J. Kvasil, and R. K. Sheline,  $^{219}\text{Fr}$ , a transitional reflection asymmetric nucleus, *Phys. Rev. C* **44**, 676 (1991).
- [47] E. Verstraelen *et al.*, Search for octupole-deformed actinium isotopes using resonance ionization spectroscopy, *Phys. Rev. C* **100**, 044321 (2019).